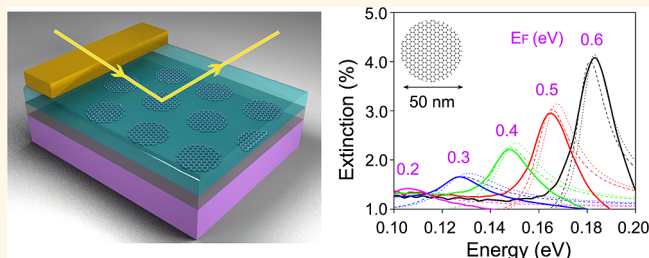


Gated Tunability and Hybridization of Localized Plasmons in Nanostructured Graphene

Zheyu Fang,^{†,‡,||} Sukosin Thongrattanasiri,^{*,||} Andrea Schlather,^{†,||} Zheng Liu,[§] Lulu Ma,[§] Yumin Wang,[†] Pulickel M. Ajayan,[§] Peter Nordlander,[†] Naomi J. Halas,[†] and F. Javier García de Abajo^{‡,*}

[†]Department of Electrical and Computer Engineering, Department of Physics and Astronomy, and Laboratory for Nanophotonics, Rice University, Houston, Texas 77005, United States, [‡]IQFR-CSIC, Serrano 119, 28006 Madrid, Spain, [§]Mechanical Engineering and Materials Science Department, Rice University, Houston, Texas 77005, United States, and ^{||}School of Physics, State Key Lab for Mesoscopic Physics, Peking University, Beijing 100871, China. ^{||}These authors contributed equally to this work.

ABSTRACT Graphene has emerged as an outstanding material for optoelectronic applications due to its high electronic mobility and unique doping capabilities. Here we demonstrate electrical tunability and hybridization of plasmons in graphene nanodisks and nanorings down to 3.7 μm light wavelength. By electrically doping patterned graphene arrays with an applied gate voltage, we observe radical changes in the plasmon energy and strength, in excellent quantitative agreement with rigorous analytical theory. We further show evidence of an unexpected increase in plasmon lifetime with growing energy. Plasmon hybridization and electrical doping in nanorings of suitably chosen nanoscale dimensions are key elements for bringing the optical response of graphene closer to the near-infrared, where it can provide a robust, integrable platform for light modulation, switching, and sensing.



KEYWORDS: plasmonics · graphene plasmons · nanophotonics · nanodisks · nanorings · optical tunability

Light manipulation at subwavelength scales benefits from interactions with electronic excitations, ranging from extended modes in micrometer-sized optical cavities down to transitions in weakly coupled atoms and small molecules. Somewhere in between, the collective electron oscillations known as plasmons¹ offer the advantage of being robust and providing fairly strong light confinement and optical field enhancement, which have triggered a plethora of applications,² for example, in optical sensing,^{3,4} cancer therapy,^{5,6} and catalysis.^{7,8} Recently, a large deal of work has been devoted to finding materials with improved plasmonic performance and fast tunability,⁹ including the use of superconductors in the sub-THz regime¹⁰ and conductive oxides in the visible and near-infrared.¹¹ However, these materials involve cryogenic environments and demanding syntheses. The electronic nature of plasmons suggests electrical tunability as a natural route toward integrable, fast plasmon

modulation, but conventional plasmonic materials such as gold and silver can only undergo mild tuning through massive charging.^{12,13}

In this context, graphene has emerged as a promising tunable material capable of sustaining plasmons when it is electrically charged.¹⁴ The plasmon energy strongly depends on the concentration of charge carriers. With no states at the Fermi level in its neutral form,¹⁴ a moderate concentration of doping charge carriers n can significantly raise the Fermi energy to high values relative to the Dirac point (e.g., $E_F = \hbar v_F (\pi n)^{1/2} = 0.5$ eV for $n = 2 \times 10^{13} \text{ cm}^{-2}$, where $v_F \approx 10^6$ m/s is the Fermi velocity in the carbon layer). Plasmons can then exist up to an energy $\sim E_F$, beyond which they are strongly quenched by interband electronic transitions.^{15,16} Evidence for graphene plasmons and their electrical tunability has been recently obtained in ribbons through THz^{17,18} and mid-infrared¹⁹ absorption spectroscopies, as well as through direct mid-infrared

* Address correspondence to j.g.deabajo@nanophotonics.es.

Received for review December 3, 2012 and accepted February 7, 2013.

Published online February 07, 2013
10.1021/nn3055835

© 2013 American Chemical Society

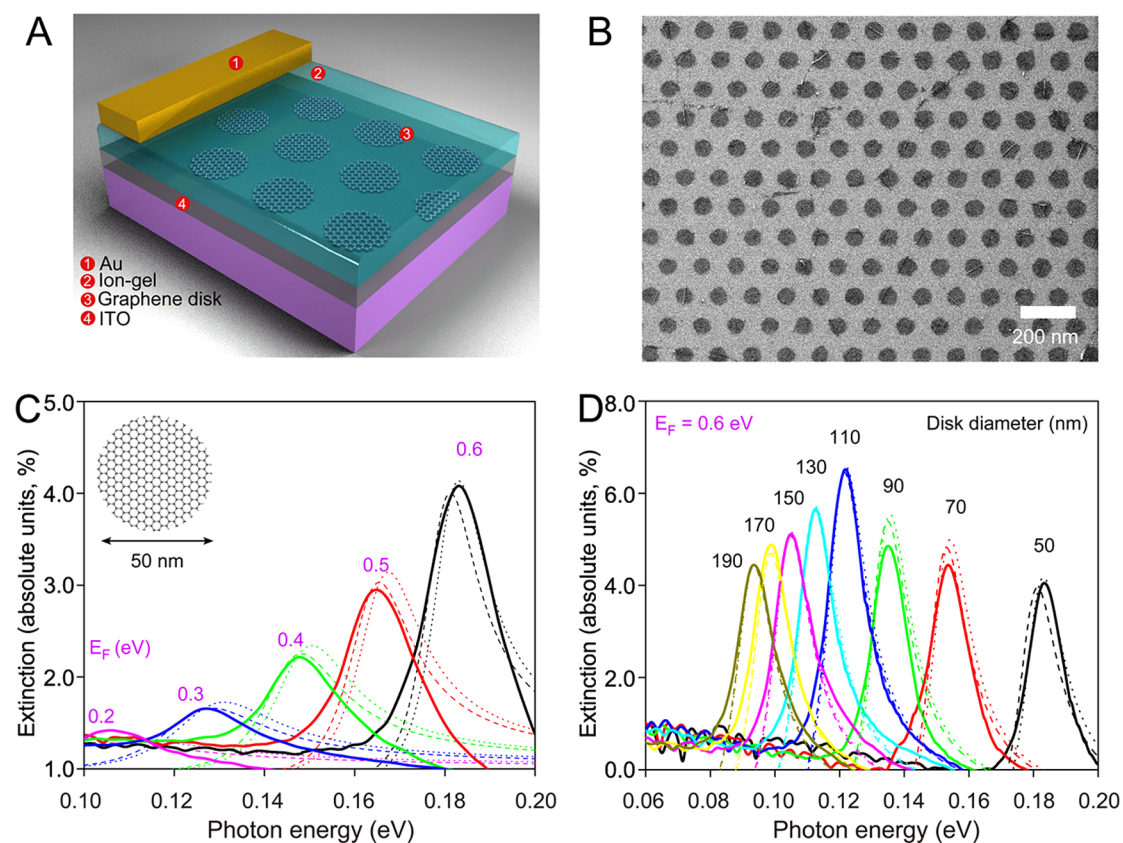


Figure 1. Electrical and geometrical tunability of graphene nanodisk plasmons. (A) Scheme of the devices used in our study, consisting of an ITO-coated silica substrate (4), on top of which we pattern an array of graphene nanodisks (3), which is in turn covered with ion gel (2).²⁵ A bias potential is applied between the ITO and a gold contact (1) to electrically dope the disks through the ion gel. (B) SEM image of a characteristic graphene sample. (C) Measured (solid curves) and calculated (dashed curves from local RPA and dotted curves from Drude; see text) extinction spectra of a 50 nm disk array under different applied voltages ΔV . The doping level is quantified through the Fermi energy E_F (see text). (D) Experimental and theoretical spectra for fixed doping ($E_F = 0.61$ eV) and varying disk diameter (indicated by labels from 50 to 190 nm). The extinction is given in % of the difference between regions with and without graphene.

near-field spatial mapping.^{20,21} Further evidence of THz interacting plasmons has been reported in graphene disks and rings of fixed intrinsic doping.^{18,22,23} Control over the damping of plasmons in a gold/graphene nanostructure has also been realized down to 3 μm wavelength.²⁴

In this article, we demonstrate control over the plasmons of graphene nanostructures through both electrical doping and plasmon hybridization. The former enables fast control over the plasmon wavelength, whereas the latter allows us to operate down to a wavelength of 3.7 μm for the antibonding modes of narrow nanorings patterned with ~ 20 nm spatial resolution (see below). The versatility of this approach can be readily extended to yield tunable plasmons in the near-infrared, provided a sufficient spatial resolution is achieved in the fabrication process.

RESULTS AND DISCUSSION

We electrically dope graphene nanodisks by sandwiching them in a double-electrode configuration, as shown in Figure 1A (see Materials and Methods). We first explore arrays of nanodisks for simultaneously

achieving electrical and geometrical tuning of their dipolar plasmons. A characteristic graphene sample is shown in the SEM image of Figure 1B, consisting of a monodisperse disk array. The measured spectra of light reflected on this device, which probes a large number of disks (spot size $\sim 10 \mu\text{m}$), exhibit extinction peaks produced by the excitation of nanodisk plasmons (Figure 1C,D, solid curves). For fixed disk size and spacing (50 and 120 nm, respectively, Figure 1C), both the plasmon energy and strength increase with applied voltage. This clearly demonstrates plasmon tunability through electrical gating. Likewise, the plasmon energy decreases with increasing disk size (Figure 1D), thus showing a characteristic red shift when considering larger structures, eventually reaching the far-infrared in micrometer-sized graphene disks.^{18,22}

In order to better understand the observed spectra, we carry out electromagnetic simulations for the same structures as in the experimental samples. Under the safe assumption of small disks compared with the light wavelength, we find closed-form analytical expressions for the extinction. Although these are rather involved (see Materials and Methods), the main plasmon characteristics

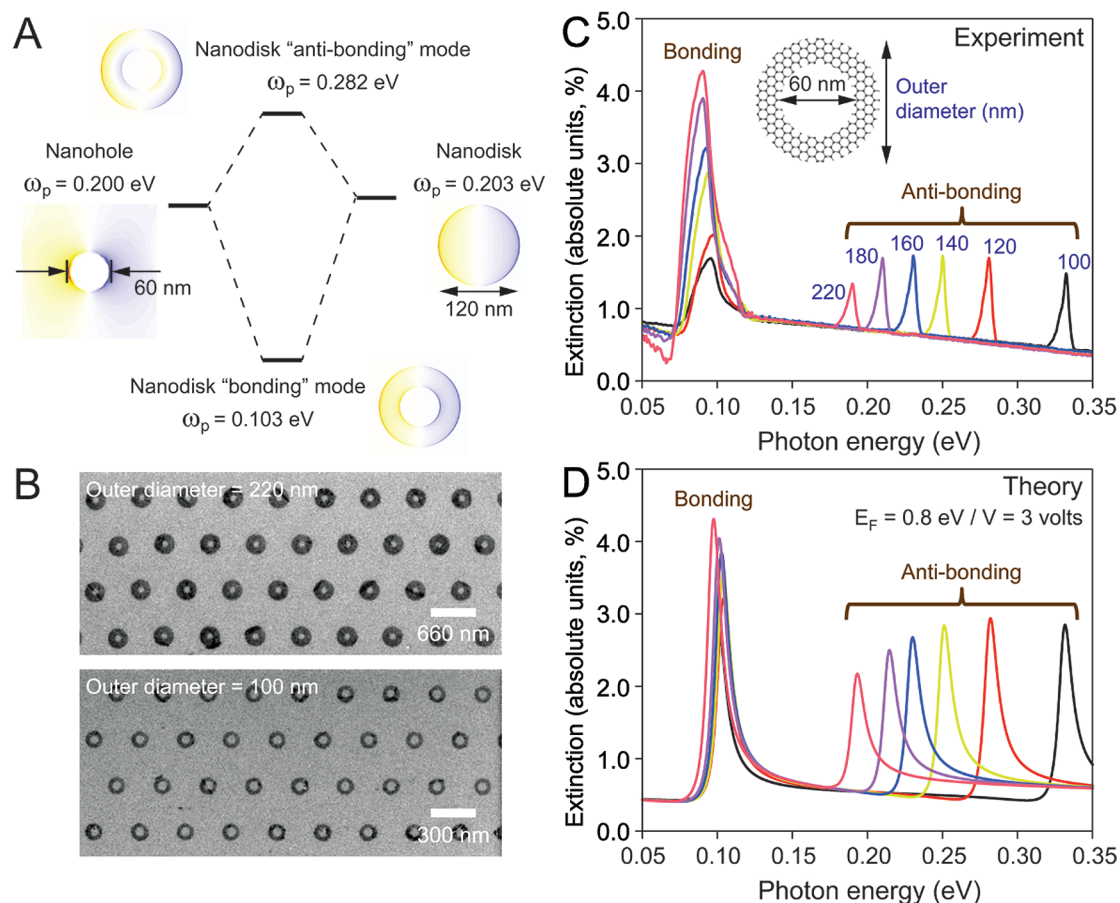


Figure 2. Bonding and antibonding hybridized plasmons in graphene nanorings. (A) Calculated plasmon-induced charges and energies showing the hybridization between disk and hole plasmons in a graphene nanodisk. (B) SEM images of nanoring samples for two different outer diameters. (C) Measured extinction spectra for fixed inner diameter (60 nm) and different outer diameters, as shown by labels. The edge-to-edge separation between disks is twice the outer diameter in all cases. (D) Calculated spectra under the conditions of (C). The Fermi energy (applied voltage) in (C) and (D) is $E_F = 0.8$ eV ($\Delta V = 3$ eV). The extinction is given in % of the difference between regions with and without graphene.

are contained in the disk polarizability, which near a plasmon resonance (labeled l) reduces to

$$\alpha(\omega) \approx D^3 \frac{A_l}{\frac{2L_l}{\varepsilon_1 + \varepsilon_2} - \frac{i\omega D}{\sigma(\omega)}} \quad (1)$$

Here, D is the disk diameter, ω is the light frequency, σ is the graphene conductivity, ε_1 and ε_2 are the dielectric constants of the ion gel and the ITO films (see Materials and Methods) defining the interface on which the disks are sitting, and the constants A_l and L_l are independent of frequency and disk size but depend on the symmetry of the plasmon under consideration. Furthermore, A_l and L_l are independent of both the dielectric environment and the exact form of σ (see Materials and Methods). These constants are determined once and for all from boundary-element method calculations,²⁶ treating the graphene as a thin conductor.²⁷ For the lowest-order dipolar disk plasmon ($l = 1$), we find $A_1 = 0.65$ and $L_1 = 12.5$. With these universal parameters for disks of any composition, our analytical theory renders the dashed curves of Figure 1C,D, using a local RPA model for the conductivity.^{27,28}

The plasmon lifetime τ is estimated from the measured DC mobility ($\mu = 780$ cm²/V·s), using the impurity-limited approximation given by $\tau = \mu E_F / eV_F$.¹⁶ Besides, the doping carrier density n is obtained from the applied voltage difference ΔV between the gold and the ITO contacts, referred to as the neutrality point, through the linear relation $n = C\Delta V/e$, where the effective capacitance density of the device $C = 2.49$ $\mu\text{F}/\text{cm}^2$ is the only fitting parameter in this article (see Materials and Methods). With this value of C , we obtain the Fermi energies shown by labels in Figure 1 and also the calculated spectra shown by broken curves. Theory and experiment agree remarkably well both in spectral shape and in the strength and energy of the plasmons. Specifically, the complex dependence of the plasmon strength on disk size for fixed E_F (Figure 1D) is successfully captured by the simple expression of eq 1, taking into account the disk spacings on the different samples (see Materials and Methods). Incidentally, for the relatively low photon energies under consideration ($\hbar\omega \ll E_F$), the simple Drude model for the conductivity, $\sigma(\omega) = [e^2/(\pi\hbar^2)]iE_F/(\omega + i\tau^{-1})$, works extremely well, as shown by the dotted curves in

Figure 1C,D. This model, combined with eq 1, predicts a plasmon energy of $\hbar\omega_p \approx \epsilon(2L_1E_F/\pi(\epsilon_1 + \epsilon_2)D)^{1/2}$, in excellent correspondence with the diameter dependence of the data shown in Figure 1D.

An additional knob with which to tailor graphene plasmons is provided by hybridization,²⁹ which we explore in Figure 2 for nanorings. In a ring, the disk dipole plasmon can interact with the plasmon of a hole, producing bonding (low-energy) and antibonding (high-energy) hybridized states, as we show in Figure 2A. We test this concept by patterning graphene ring arrays of fixed inner diameter (60 nm) but varying outer diameter. SEM images of two samples are shown in Figure 2B. The resulting extinction spectra (Figure 2C) show a bonding plasmon at nearly constant energy slightly below 0.1 eV, accompanied by an antibonding plasmon displaying a dramatic blue shift as the ring becomes narrower. This behavior is well reproduced by our theory with a single choice of Fermi energy $E_F = 0.8$ eV for all spectra (Figure 2D). Interestingly, the antisymmetric charge alignment across the ring for the antibonding state pushes this mode toward relatively high energy ~ 0.33 eV. Actually, the antibonding plasmon reaches the near-infrared at $2.8 \mu\text{m}$ wavelength for rings of 80 nm outer diameter (see Materials and Methods), for which even minor fabrication imperfections can significantly modify ensemble measurements of this kind (notice that both the observed bonding and antibonding features are decreasing in strength with decreasing ring size; this is in contrast to the behavior predicted by theory for the antibonding mode, presumably as a result of the degradation of the quality of the rings as they are made smaller; cf. the two images of Figure 2B).

The lifetime of disk plasmons is in excellent agreement with the impurity-limited DC estimate (Figure 3, $E_F = 0.61$ eV data and gray dashed line). However, the observed bonding plasmon lifetimes for rings, obtained from Figure 2C and represented in Figure 3 (open squares around 0.1 eV), are substantially reduced due to morphological plasmon shifts that are captured as an increased broadening in our ensemble measurements. Importantly, the observed lifetimes are clearly longer for the higher energy antibonding features than for the bonding modes. For the quality of the graphene used in the experiments, with a mobility $\mu = 780 \text{ cm}^2/\text{V}\cdot\text{s}$, the main source of decoherence is scattering from impurities. Our data indicate that this mechanism is overestimated in the DC impurity model (Figure 3, black dashed line) and increasingly so as the photon energy gets higher. This is consistent with the expected behavior of the coupling matrix elements between the plasmons and electron–hole pair excitations mediated by impurity scattering, which should decrease in strength with increasing plasmon energy. However, the presented series of measured lifetimes is incomplete, as it is constructed from the available observed plasmons, so that it has a gap between 0.1 and 0.2 eV. From the above argument, it seems plausible that

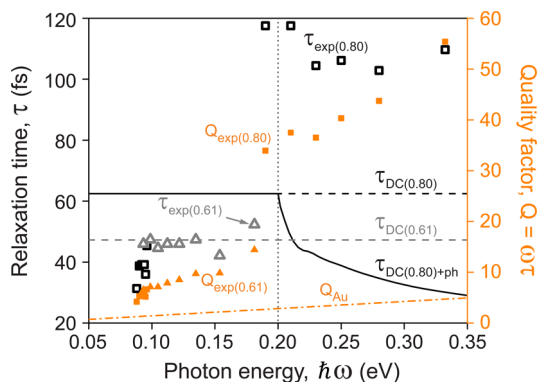


Figure 3. Graphene plasmon lifetime and quality factor. Measured plasmon lifetime (left vertical scale) determined from the width of the spectral features in Figure 1D ($\tau_{\text{exp},0.61}$, $E_F = 0.61$ eV, open triangles) and Figure 2C ($\tau_{\text{exp},0.8}$, $E_F = 0.8$ eV, open squares) and compared with both the lifetime estimated from the measured DC mobility $\mu = 780 \text{ cm}^2/\text{V}\cdot\text{s}$ ($\tau_{\text{DC}} = \mu E_F / e v_F^2$, dashed lines) and the correction to the lifetime produced by excitation of optical phonons ($\tau_{\text{DC}+\text{ph}}$, solid curve, adapted from ref 16). The measured quality factor of graphene plasmons (Q_{exp} , solid symbols, right scale) is compared with that of nanostructured gold (Q_{Au} , dot-dashed curve), estimated from the gold bulk decoherence time $\tau_{\text{Au}} \approx 9.3 \text{ fs}$.³⁰

the lifetime increases with plasmon energy from ~ 40 fs at 0.1 eV to ~ 120 fs in the data point slightly below 0.2 eV. Above 0.2 eV, we observe what seems to be a departure from this growing trend in the lifetime, which is compatible with the presence of additional losses produced by coupling to optical phonons, although this reduction is smaller than estimated from the Kubo formula¹⁶ (Figure 3, solid curve). The resulting quality factors ($Q = \text{plasmon energy divided by plasmon width}$, Figure 3, right scale) are well above what is expected for gold plasmons in small particles (see Materials and Methods), as estimated from the measured lifetime of $\sim 9.3 \text{ fs}$.³⁰ Finite size corrections are expected to be much more important for the antibonding plasmon, which predominantly involves charge oscillations across the ring wall, than for the bonding plasmon, which involves charge oscillations along the whole ring structure (see charge insets in Figure 2A). Interestingly, in the present system, the electron mean free path $v_F\tau$ is around 50 nm, which is larger than the width of the ring walls of the smallest rings in the experiment.

CONCLUSIONS

Localized graphene plasmons decay primarily by producing electron–hole pairs, which can have potential application in infrared light harvesting and spectral photodetection.³¹ The extraordinary light confinement of these plasmons (the studied nanodisks are over 100 times smaller than the incident light wavelength) has great potential for molecular sensing based upon enhanced infrared absorption. These properties benefit from the electrical tunability of graphene, which, as demonstrated in our study, provides an unprecedentedly direct approach to full light modulation and optical switching down to $3.7 \mu\text{m}$ wavelength and below.

Additionally, graphene plasmons can be tuned toward higher energies by using other shapes containing narrower structures, such as tapered ribbons, and also by

increasing the level of doping,³² thus extending the optical tunability of graphene toward spectral regions of interest for communications and data processing.

MATERIALS AND METHODS

Sample Preparation, Electrical Doping, and Optical Characterization.

High-quality large-area graphene films were grown using an optimized liquid precursor chemical vapor deposition method,³³ determined to be single-layer through Raman measurements, transferred onto an ITO/oxide/Si substrate (20 nm ITO film sputtered on a commercial 285 nm oxidized Si on Si substrate), patterned into nanodisk and nanoring arrays using electron-beam lithography and 15 s oxygen plasma etching, and covered with ion gel (~100 nm thick film) following the procedure described in ref 25. The ITO and ion gel layer thicknesses were determined through ellipsometry. A top-gate gold contact was fabricated on the ion gel layer (see Figure 1A). The area of each array was about $20 \times 20 \mu\text{m}^2$. We fabricated arrays of disks with the following combinations of diameter D and (center-to-center) lattice spacing a (values of (D, a) in nm): (50, 120), (70, 150), (90, 180), (110, 200), (130, 250), (150, 300), (170, 350), and (190, 400). We also fabricated arrays of rings with fixed 60 nm inner diameter, outer diameters in the 100–220 nm range, and center-to-center distance equal to three times the outer diameter in each case. We confirmed that the mobility of unpatterned graphene areas was 2100 and 780 $\text{cm}^2/\text{V}\cdot\text{s}$ before and after ion gel deposition, respectively, in accordance with literature.^{34,35} Thanks to the high capacitance density of the ion gel (fitted to $2.49 \mu\text{F}/\text{cm}^2$; see next section), the Fermi energy of the graphene nanostructure could be tuned from 0.2 to 0.6 eV by applying a bias voltage from 0.2 to 1.73 V between the top gold gate and the ITO bottom gate. We measured the reflected light intensities in sample regions with (I_1) and without (I_2) graphene using a Fourier transform infrared spectrometer (Bruker v80v) coupled to an infrared microscope ($36\times$ objective) under ambient conditions. This directly yielded extinction spectra given by $1 - I_1/I_2$.

Determination of the Capacitance Density. The effective capacitance density C is the only fitting parameter in this paper. The rest of the electrical and geometrical parameters were determined from experimental measurements (see above), whereas dielectric data were taken from the literature (see next paragraph). In determining C , it was assumed that we were in the linear electrostatic doping regime, so that the charge carrier density was given by $n = C\Delta V/e$, where ΔV was the potential applied between the gold and ITO electrodes (referred to the charge-neutrality point), which was varied between 0.2 and 3.0 V (see specific values in Figures 1 and 2). The latter was determined from I – V characterization measurements. The Fermi energy was related to n through $E_F = \hbar v_F(\pi n)^{1/2}$,¹⁴ where $v_F = 10^6$ m/s is the Fermi velocity. We obtained a value of $C = 2.49 \mu\text{F}/\text{cm}^2$ by adjusting it to achieve the best overall fit between the extinction measurements and the calculated spectra. The calculations were performed using the theoretical model that we describe in next paragraph. This value of C is on the same order of magnitude as that found in previous reports for similar devices.^{34,35} It is remarkable that a single value of C correctly yields the position of the observed maxima and the relative height of the peaks for both disks and rings, as well as the widths of the plasmons for disks (as determined from the measured mobility).

Theoretical Model. The graphene disks and rings examined in this work have diameters much smaller than the light wavelength at which they support plasmons (37 to several hundred times smaller for the geometrical and doping parameters considered here). This allows us to safely describe each of them in the electrostatic limit. The graphene lies at the interface between ion gel and ITO media. It is then useful to write a self-consistent equation for the scalar electric potential ϕ (associated with the electric field upon illumination at

frequency ω) in the plane of the disk/ring as

$$\phi(\mathbf{R}) = \phi^{\text{ext}}(\mathbf{R}) + \left(\frac{2}{\epsilon_1 + \epsilon_2}\right) \frac{i}{\omega} \int \frac{d^2\mathbf{R}'}{|\mathbf{R} - \mathbf{R}'|} \nabla' \cdot \sigma(\mathbf{R}', \omega) \nabla' \phi(\mathbf{R}') \quad (2)$$

where ϕ^{ext} is the external potential (incident light), \mathbf{R} is the coordinate vector in the plane of the graphene, $\sigma(\mathbf{R}, \omega)$ is the position and frequency-dependent 2D conductivity of the carbon layer, and an $\exp(-i\omega t)$ time dependence is understood. The integral in eq 2 represents the potential produced by the induced charges, expressed in terms of the induced current $j = -\sigma \nabla \phi$ through the continuity equation as $(-i/\omega) \nabla \cdot j$. The factor of $2/(\epsilon_1 + \epsilon_2)$ rigorously corrects the $1/r$ Coulomb potential in free space to account for the effect of the dielectrics when the charges are placed right at a planar interface. We work within the local approximation, which works well for structures wider than a few tens of nanometers.³⁶ We further assume an effective homogeneous doping of the disk/ring,³⁷ so that $\sigma(\mathbf{R}, \omega) = f(\mathbf{R})\sigma(\omega)$, where $f(\mathbf{R})$ is an *occupation* function that is 1 on the graphene area and vanishes elsewhere. At this point, we introduce the dimensionless coordinate vector $\vec{\theta} = \mathbf{R}/D$, where D is the disk (or outer ring) diameter. Incorporating these elements in eq 2, we find

$$\phi(\vec{\theta}) = \phi^{\text{ext}}(\vec{\theta}) + \eta \int \frac{d^2\vec{\theta}'}{|\vec{\theta} - \vec{\theta}'|} \nabla' \cdot f(\vec{\theta}') \nabla' \phi(\vec{\theta}') \quad (3)$$

where

$$\eta = \frac{i\sigma(\omega)}{\omega D} \frac{2}{\epsilon_1 + \epsilon_2} \quad (4)$$

is a dimensionless parameter. In the absence of external fields, eq 3 reduces to a Hermitian eigensystem of real eigenvalues $1/\eta_l$, some of which are associated with plasmons of the disk/ring. The self-consistent potential that solves eq 3 can thus be expressed as a sum over the corresponding eigenfunctions ϕ_l . It is important to stress that this eigenvalue problem has a pure geometrical form, independent of the graphene response, which is fully contained in the parameter η (i.e., the real constants η_l are independent of the quality of the graphene, the level of doping, the frequency, and the size of the disk/ring). They only depend on the geometry, and we calculate them once and for all for a disk and also for each ratio of the inner-to-outer diameter ratio in the rings (see Table 1).

We further assume that the disks/rings are sufficiently far away from each other to safely be described through their dipolar polarizability α . Using the noted eigenfunction expansion, we find, after some algebra,

$$\alpha(\omega) = D^3 \sum_l \frac{A_l}{\frac{2L_l}{\epsilon_1 + \epsilon_2} - \frac{i\omega D}{\sigma(\omega)}} \quad (5)$$

where A_l are real positive geometry-dependent (but size- and material-independent) expansion coefficients and $L_l = -1/\eta_l$. These dimensionless constants are listed in Table 1 for the relevant modes in the disks/rings studied in this work, characterized by $L_l > 0$ values. (Incidentally, small variations of the parameters listed in this table are possible depending on the ratio of the thickness used for the graphene, which we fix here to 0.5 nm.) In particular, the disks are modeled using just the lowest-order dipolar plasmon, whereas for the rings, l runs over their two plasmons of bonding and antibonding nature. Other resonances exist outside the studied energy range, supplemented by nonresonant modes associated with $L_l < 0$, which contribute to a background polarizability that turns out to be negligible, as we show next.

The accuracy of this polarizability model is illustrated in Figure 4. The solid curve is the extinction cross section σ^{ext} of

TABLE 1. Universal Geometrical Constants Entering Equation 5, Calculated for the Relevant Disk and Ring Modes Described in This Work^a

mode	D_{in}/D_{out}	L_l	A_l	
disk dipole	NA	12.5	0.65	
	ring (bonding)	0.273	11.7	0.45
		0.333	10.3	0.42
		0.375	9.5	0.39
		0.429	8.5	0.36
		0.5	7.3	0.32
		0.6	5.8	0.26
0.75	4.0	0.17		
ring (antibonding)	0.273	46	0.14	
	0.333	47	0.17	
	0.375	48	0.18	
	0.429	50	0.19	
	0.5	55	0.19	
	0.6	64	0.17	
	0.75	87	0.12	

^a For the rings, the values depend on the ratio of inner-to-outer diameters D_{in}/D_{out} .

one of the rings calculated from Maxwell's equations, using the boundary-element method²⁶ and modeling the graphene as a thin film, as explained in refs 27 and 38. The dashed curve corresponds to the analytical model

$$\sigma^{\text{ext}} = 4\pi k \text{Im}\{\alpha\} \quad (6)$$

where $k = \omega/c$ is the free-space light wave vector and α is given by eq 5. We obtain excellent agreement between numerical and analytical calculations by adjusting the parameters A_l and L_l associated with the bonding and antibonding features to the values shown in Table 1 for $D_{in}/D_{out} = 60/160 = 0.375$.

The reflection (r) and transmission (t) coefficients of the $\varepsilon_1/\varepsilon_2$ interface decorated with the disk/ring array are then obtained by extending the method described in ref 31. For light incident from medium 1, we find

$$\begin{aligned} r_s &= r_s^0 + \frac{iS_s(1+r_s^0)}{1/\alpha - G_s}, & t_s &= t_s^0 + \frac{iS_s t_s^0}{1/\alpha - G_s}, \\ r_p &= r_p^0 + \frac{iS_p(1-r_p^0)}{1/\alpha - G_p}, & t_p &= t_p^0 + \frac{iS_p t_p^0}{1/\alpha - G_p}, \end{aligned}$$

for s and p polarizations, where

$$\begin{aligned} r_s^0 &= \frac{k_{\perp 1} - k_{\perp 2}}{k_{\perp 1} + k_{\perp 2}}, & t_s^0 &= \frac{2k_{\perp 1}}{k_{\perp 1} + k_{\perp 2}}, \\ r_p^0 &= \frac{\varepsilon_2 k_{\perp 1} - \varepsilon_1 k_{\perp 2}}{\varepsilon_2 k_{\perp 1} + \varepsilon_1 k_{\perp 2}}, & t_p^0 &= \frac{2\sqrt{\varepsilon_1 \varepsilon_2} k_{\perp 1}}{\varepsilon_2 k_{\perp 1} + \varepsilon_1 k_{\perp 2}} \end{aligned}$$

are the Fresnel coefficients of the graphene-free interface,

$$\begin{aligned} S_s &= \frac{4\pi}{A} \frac{k^2}{k_{\perp 1} + k_{\perp 2}}, & G_s &\approx \frac{g}{a^3} \varepsilon_1 + \varepsilon_2 + iS_s, \\ S_p &= \frac{4\pi}{A} \frac{k_{\perp 1} k_{\perp 2}}{\varepsilon_2 k_{\perp 1} + \varepsilon_1 k_{\perp 2}}, & G_p &\approx \frac{g}{a^3} \varepsilon_1 + \varepsilon_2 + iS_p, \end{aligned}$$

$k_{\perp j} = (k^2 \varepsilon_j - k_{\parallel}^2 + i0^+)^{1/2}$ (with $\text{Im}\{k_{\perp j}\} > 0$) and $k_{\parallel} = k \sin \theta$ are the perpendicular and parallel components of the wave vector in media $j = 1, 2$ for an angle of incidence θ ($\theta = 0$ in this work), a is the lattice period, A is the area of the unit cell, and g is a dimensionless constant that depends on the lattice symmetry. For the hexagonal arrays under consideration, we have $A = \sqrt{3}a^2/2$ and $g = 5.52$. Because the spacing is much smaller than the light wavelength, we neglect diffracted beams (i.e., we assume that $k_{\parallel} = 0$ is conserved across the interface).

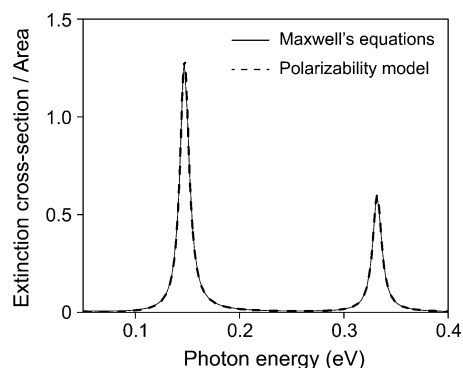


Figure 4. Accuracy of the polarizability model. We show the normal-incidence extinction cross section of a free-standing graphene ring of $D_{out} = 160$ nm ($D_{in} = 60$ nm) outer (inner) diameter, calculated by solving Maxwell's equations using the local RPA conductivity of eq 7 (solid curve), as compared with the analytical model of eqs 5 and 6 (dashed curve). The Fermi energy and the mobility are fixed to $E_F = 0.8$ eV and $\mu = 780$ cm²/V s, respectively. The cross section is normalized to the graphene area $\pi(D_{out}^2 - D_{in}^2)/4$.

Finally, we calculate the reflection and transmission coefficients of the entire structure using a Fabry–Perot-type model³⁹ to include the silica layer (285 nm), the Si substrate, and the interface between ion gel (100 nm) and air, as well as the one between ITO (20 nm) and silica. Other dielectric and geometrical parameters are given in the experimental paragraphs.

Dielectric Parameters. We have used tabulated optical data for Si,⁴⁰ whereas the ion gel is described by a nondispersive permittivity $\varepsilon = 1.82$.⁴¹ For oxidized Si, we assume a constant $\varepsilon = 2.1$, as signatures of silica optical phonons are not observed either in the spectra of Figures 1 and 2 or in the reflectivity that we have additionally measured from a bare oxidized Si substrate. We attribute the lack of well-defined phonons to the complex chemical structure of the oxidized Si, possibly involving a complex fine mixture of different oxide states that present local variations with respect to the stoichiometry of silica. The optical response of ITO deserves further discussion: thick ITO films have been reported to exhibit metallic behavior in the mid-infrared, but a severe depletion of charge carrier concentration has been reported as the film is made thinner, down by a factor of 3 at 150 nm;⁴² our ITO film is considerably thinner (~ 20 nm), and therefore, we expect an even more dramatic reduction in charge carriers; this is consistent with the fact that we have measured only an average 15% change in reflectance in the mid-infrared range when our ~ 20 nm ITO film is deposited on the oxidized Si substrate, thus indicating that the ITO does not have a high concentration of charge carriers, and therefore, the real part of the permittivity must be still positive and the imaginary part small. Additionally, the film was annealed at 475 °C under a pressure of 350 mTorr after evaporation; this process is expected to change the optical properties of the film from those of crystalline ITO. From these considerations, we have adopted for the ITO permittivity a value observed in the near-infrared, $\varepsilon = 2.3 + 0.5i$, which is supplemented by a small imaginary part to phenomenologically account for mid-infrared losses due to a small concentration of charge carriers.

Description of the Graphene. We describe the local, frequency-dependent graphene conductivity $\sigma(\omega)$ in the zero-parallel wave vector limit of the random-phase approximation (local RPA), including the effect of finite temperature ($T = 300$ K). More precisely⁴³

$$\begin{aligned} \sigma(\omega) &= \frac{2e^2 T}{\pi \hbar} \frac{i}{\omega + i\tau^{-1}} \log[2\cosh(E_F/2k_B T)] \\ &+ \frac{e^2}{4\hbar} \left[H(\omega/2) + \frac{4i\omega}{\pi} \int_0^\infty d\varepsilon \frac{H(\varepsilon) - H(\omega/2)}{\omega^2 - 4\varepsilon^2} \right] \quad (7) \end{aligned}$$

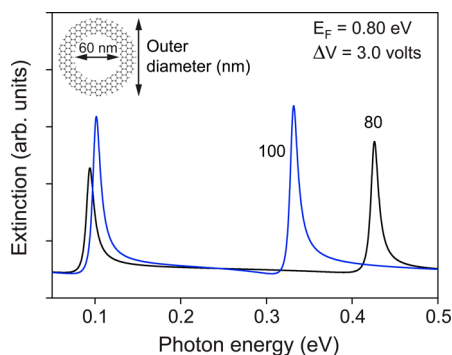


Figure 5. Near-infrared plasmons in graphene. We show the extinction spectrum predicted for nanorings of outer (inner) diameter equal to $D_{\text{out}} = 80$ nm ($D_{\text{in}} = 60$ nm) under the same conditions as in Figure 2D, from which the $D_{\text{out}} = 100$ nm spectrum is reproduced for comparison.

where

$$H(\varepsilon) = \frac{\sinh(\hbar\varepsilon/k_B T)}{\cosh(E_F/k_B T) + \cosh(\hbar\varepsilon/k_B T)}$$

We have used this local RPA response to obtain the dashed curves of Figure 1 and the theory of Figure 2. The dephasing time used in the calculated spectra is estimated from the measured DC mobility of our samples ($\mu = 780$ cm²/V·s) through the expression $\tau = \mu\hbar(n\pi)^{1/2}/e v_F$,¹⁶ where $v_F = 10^6$ m/s is the Fermi velocity of graphene, and $n = (E_F/\hbar v_F)^2/\pi$ is the charge carrier density.¹⁴

Simpler analytical expressions are obtained by neglecting both interband transitions (second term in eq 7) and the effect of temperature ($T = 0$). Under these approximations, the conductivity of eq 7 reduces to the Drude model

$$\sigma(\omega) = \frac{e^2 E_F}{\pi \hbar^2} \frac{i}{\omega + i\tau^{-1}} \quad (8)$$

which only describes intraband transitions. We have used the Drude model to obtain the dotted curves of Figure 1.

Analytical Expression for the Plasmon Energies. The plasmons correspond to the solutions of eq 3 in the absence of external fields, which are signaled by the condition $\eta = \eta_i$. Introducing eq 4 into this expression, and using eq 8 for σ (Drude model), we find the plasmon frequencies

$$\omega_l = \frac{e}{\hbar} \sqrt{\frac{2L_l E_F}{\pi(\varepsilon_1 + \varepsilon_2)D}} - \frac{i}{2\tau} \quad (9)$$

where the last term is imaginary and accounts for the finite plasmon lifetime τ . Plasmon frequencies for disks/rings can be readily obtained from eq 9 by plugging the values of L_l listed in Table 1. This expression shows that both the level of doping (E_F) and the size of the structure (D) can be used to tune the frequency. This is in contrast to conventional noble metal nanoparticles, for which similar levels of doping as used in graphene (*i.e.*, similar surface carrier densities n) produce insignificant effects, and the plasmon energy is size-independent when the diameter is much smaller than the wavelength (*i.e.*, in the absence of retardation effects) and above the cutoff of nonlocal effects (at ~ 10 nm in gold and silver⁴⁴).

Near-Infrared Plasmons in Narrow Rings. We plot in Figure 5 calculated spectra for rings of 80 and 100 nm outer diameter, corresponding to ring widths of 10 and 20 nm, respectively. The 100 nm rings are the smallest ones that we have measured, for which theory and experiment are in good agreement, as shown in Figure 2 under the same doping conditions as considered in Figure 5. The 80 nm rings, which are within the range of validity of our theory (narrower rings require incorporating quantum finite-size effects³⁶), exhibit an antibonding plasmon feature at an energy of 0.44 eV (*i.e.*, a wavelength of 2.8 μ m). This confirms that highly doped, narrow graphene structures can confine near-infrared plasmons, thus posing the challenge of a

demanding, but feasible, fabrication precision to reduce size-dispersion effects.

Quality Factor of Plasmons in Au Nanostructures. Ignoring nonlocal effects, a small gold particle (*i.e.*, sufficiently small to neglect retardation) can be approximately described by a Drude dielectric function $\varepsilon(\omega) = \varepsilon_b - \omega_p^2/(\omega(\omega + i\gamma))$, where $\varepsilon_b = 9$, $\hbar\omega_p = 9$ eV, and $\hbar\gamma = 0.07$ eV (*i.e.*, $\tau = 1/\gamma = 9.3$ fs), as deduced from optical data.³⁰ In the electrostatic limit, the plasmon resonances are obtained by equating $\varepsilon(\omega) = C$, where C is a real number that depends on the geometry and the permittivity of the host. From this equation, we find the plasmon frequency to be $\omega = (\omega_p^2/(\varepsilon_b - C) - \gamma^2/4)^{1/2} - i\gamma/2$, and since $\gamma \ll \text{Re}\{\omega\}$, we can approximate $\omega = \omega_p/(\varepsilon_b - C)^{1/2} - i\gamma/2$. That is, $\text{Im}\{\omega\}$ (and therefore the plasmon lifetime, as well) is independent of particle shape under these approximations.

Conflict of Interest: The authors declare no competing financial interest.

Acknowledgment. Z.F., Y.W., A.S., P.N., and N.J.H. are supported by the Robert A. Welch Foundation (C-1220 and C-1222), the Office of Naval Research (N00014-10-1-0989), and the DoD NSSEFF (N00244-09-1-0067); S.T. and F.J.G.A. are supported by the Spanish MEC (MAT2010-14885 and Consolider NanoLight.es) and the European Commission (FP7-ICT-2009-4-248909-LIMA); Z.L., L.M., and P.M.A. are supported by the office of Naval Research through the MURI program on graphene.

REFERENCES AND NOTES

- Raether, H. *Surface Plasmons on Smooth and Rough Surfaces and on Gratings*; Springer-Verlag: Berlin, 1988; Vol. 111.
- Polman, A. *Plasmonics Applied*. *Science* **2008**, *322*, 868–869.
- Nie, S.; Emory, S. R. Probing Single Molecules and Single Nanoparticles by Surface-Enhanced Raman Scattering. *Science* **1997**, *275*, 1102–1106.
- Rodríguez-Lorenzo, L.; Álvarez-Puebla, R. A.; Pastoriza-Santos, I.; Mazzucco, S.; Stéphan, O.; Kociak, M.; Liz-Marzán, L. M.; García de Abajo, F. J. Zeptomol Detection through Controlled Ultrasensitive Surface-Enhanced Raman Scattering. *J. Am. Chem. Soc.* **2009**, *131*, 4616–4618.
- Qian, X.; Peng, X.-H.; Ansari, D. O.; Yin-Goen, Q.; Chen, G. Z.; Shin, D. M.; Yang, L.; Young, A. N.; Wang, M. D.; Nie, S. *In Vivo* Tumor Targeting and Spectroscopic Detection with Surface-Enhanced Raman Nanoparticle Tags. *Nat. Biotechnol.* **2008**, *26*, 83–90.
- Hirsch, L.; Stafford, R.; Bankson, J.; Sershen, S.; Rivera, B.; Price, R.; Hazle, J.; Halas, N.; West, J. Nanoshell-Mediated Near-Infrared Thermal Therapy of Tumors under Magnetic Resonance Guidance. *Proc. Natl. Acad. Sci. U.S.A.* **2003**, *100*, 13549–13554.
- Asahi, R.; Morikawa, T.; Ohwaki, T.; Aoki, K.; Taga, Y. Visible-Light Photocatalysis in Nitrogen-Doped Titanium Oxides. *Science* **2001**, *293*, 269–271.
- Kamat, P. V. Photophysical, Photochemical and Photocatalytic Aspects of Metal Nanoparticles. *J. Phys. Chem. B* **2002**, *106*, 7729–7744.
- Ben-Abdallah, P.; Biehs, S. A.; Joulain, K. Low-Loss Plasmonic Metamaterials. *Science* **2011**, *331*, 290–291.
- Tsiatmas, A.; Buckingham, A. R.; Fedotov, V. A.; Wang, S.; Chen, Y.; de Groot, P. A. J.; Zheludev, N. I. Superconducting Plasmonics and Extraordinary Transmission. *Appl. Phys. Lett.* **2010**, *97*, 111106.
- Feigenbaum, E.; Diest, K.; Atwater, H. A. Unity-Order Index Change in Transparent Conducting Oxides at Visible Frequencies. *Nano Lett.* **2010**, *10*, 2111–2116.
- Chapman, R.; Mulvaney, P. Electro-Optical Shifts in Silver Nanoparticle Films. *Chem. Phys. Lett.* **2001**, *349*, 358–362.
- Hirakawa, T.; Kamat, P. V. Photoinduced Electron Storage and Surface Plasmon Modulation in Ag@TiO₂ Clusters. *Langmuir* **2004**, *20*, 5645–5647.
- Castro Neto, A. H.; Guinea, F.; Peres, N. M. R.; Novoselov, K. S.; Geim, A. K. The Electronic Properties of Graphene. *Rev. Mod. Phys.* **2009**, *81*, 109–162.

15. Wunsch, B.; Stauber, T.; Sols, F.; Guinea, F. Dynamical Polarization of Graphene at Finite Doping. *New J. Phys.* **2006**, *8*, 318.
16. Jablan, M.; Buljan, H.; Soljačić, M. Plasmonics in Graphene at Infrared Frequencies. *Phys. Rev. B* **2009**, *80*, 245435.
17. Ju, L.; Geng, B.; Horng, J.; Girit, C.; Martin, M.; Hao, Z.; Bechtel, H. A.; Liang, X.; Zettl, A.; Shen, Y. R.; *et al.* Graphene Plasmonics for Tunable Terahertz Metamaterials. *Nat. Nanotechnol.* **2011**, *6*, 630–634.
18. Yan, H.; Li, Z.; Li, X.; Zhu, W.; Avouris, P.; Xia, F. Infrared Spectroscopy of Tunable Dirac Terahertz Magneto-Plasmons in Graphene. *Nano Lett.* **2012**, *12*, 3766–3771.
19. Fei, Z.; Andreev, G. O.; Bao, W.; Zhang, L. M.; McLeod, A. S.; Wang, C.; Stewart, M. K.; Zhao, Z.; Dominguez, G.; Thiemens, M.; *et al.* Infrared Nanoscopy of Dirac Plasmons at the Graphene–SiO₂ Interface. *Nano Lett.* **2011**, *11*, 4701–4705.
20. Chen, J.; Badioli, M.; Alonso-González, P.; Thongrattanasiri, S.; Huth, F.; Osmond, J.; Spasenović, M.; Centeno, A.; Pesquera, A.; Godignon, P.; *et al.* Optical Nano-Imaging of Gate-Tunable Graphene Plasmons. *Nature* **2012**, *487*, 77–81.
21. Fei, Z.; Rodin, A. S.; Andreev, G. O.; Bao, W.; McLeod, A. S.; Wagner, M.; Zhang, L. M.; Zhao, Z.; Thiemens, M.; Dominguez, G.; *et al.* Gate-Tuning of Graphene Plasmons Revealed by Infrared Nano-Imaging. *Nature* **2012**, *487*, 82–85.
22. Yan, H.; Li, X.; Chandra, B.; Tulevski, G.; Wu, Y.; Freitag, M.; Zhu, W.; Avouris, P.; Xia, F. Tunable Infrared Plasmonic Devices Using Graphene/Insulator Stacks. *Nat. Nanotechnol.* **2012**, *7*, 330–334.
23. Yan, H.; Xia, F.; Li, Z.; Avouris, P. Plasmonics of Coupled Graphene Micro-Structures. *arXiv* **2012**, 1205.6841.
24. Emani, N. K.; Chung, T.-F.; Ni, X.; Kildishev, A. V.; Chen, Y. P.; Boltasseva, A. Electrically Tunable Damping of Plasmonic Resonances with Graphene. *Nano Lett.* **2012**, *12*, 5202–5206.
25. Chen, C. F.; Park, C. H.; Boudouris, B. W.; Horng, J.; Geng, B.; Girit, C.; Zettl, A.; Crommie, M. F.; Segalman, R. A.; Louie, S. G.; *et al.* Controlling Inelastic Light Scattering Quantum Pathways in Graphene. *Nature* **2011**, *471*, 617–620.
26. Garca de Abajo, F. J.; Howie, A. Retarded Field Calculation of Electron Energy Loss in Inhomogeneous Dielectrics. *Phys. Rev. B* **2002**, *65*, 115418.
27. Koppens, F. H. L.; Chang, D. E.; García de Abajo, F. J. Graphene Plasmonics: A Platform for Strong Light–Matter Interactions. *Nano Lett.* **2011**, *11*, 3370–3377.
28. Falkovsky, L. A.; Varlamov, A. A. Space–Time Dispersion of Graphene Conductivity. *Eur. Phys. J. B* **2007**, *56*, 281.
29. Prodan, E.; Radloff, C.; Halas, N. J.; Nordlander, P. Hybridization Model for the Plasmon Response of Complex Nanostructures. *Science* **2003**, *302*, 419–422.
30. Johnson, P. B.; Christy, R. W. Optical Constants of the Noble Metals. *Phys. Rev. B* **1972**, *6*, 4370–4379.
31. Thongrattanasiri, S.; Koppens, F. H. L.; García de Abajo, F. J. Complete Optical Absorption in Periodically Patterned Graphene. *Phys. Rev. Lett.* **2012**, *108*, 047401.
32. Khrapach, I.; Withers, F.; Bointon, T. H.; Polyushkin, D. K.; Barnes, W. L.; Russo, S.; Craciun, M. F.; Monica, F. Novel Highly Conductive and Transparent Graphene-Based Conductors. *Adv. Mater.* **2012**, *24*, 2844–2849.
33. Li, X.; Cai, W.; An, J.; Kim, S.; Nah, J.; Yang, D.; Piner, R.; Velamakanni, A.; Jung, I.; Tutuc, E.; *et al.* Large-Area Synthesis of High-Quality and Uniform Graphene Films on Copper Foils. *Science* **2009**, *324*, 1312–1314.
34. Cho, J. H.; Lee, J.; Xia, Y.; Kim, B.; He, Y.; Renn, M. J.; Lodge, T. P.; Frisbie, C. D. Printable Ion-Gel Gate Dielectrics for Low-Voltage Polymer Thin-Film Transistors on Plastic. *Nat. Mater.* **2008**, *7*, 900–906.
35. Kim, B. J.; Jang, H.; Lee, S.-K.; Hong, B. H.; Ahn, J.-H.; Cho, J. H. High-Performance Flexible Graphene Field Effect Transistors with Ion Gel Gate Dielectrics. *Nano Lett.* **2010**, *10*, 3464–3466.
36. Thongrattanasiri, S.; Manjavacas, A.; García de Abajo, F. J. Quantum Finite-Size Effects in Graphene Plasmons. *ACS Nano* **2012**, *6*, 1766–1775.
37. Thongrattanasiri, S.; Silveiro, I.; García de Abajo, F. J. Plasmons in Electrostatically Doped Graphene. *Appl. Phys. Lett.* **2012**, *100*, 201105.
38. Vakil, A.; Engheta, N. Transformation Optics Using Graphene. *Science* **2011**, *332*, 1291–1294.
39. Stefanou, N.; Yannopoulos, V.; Modinos, A. MULTEM 2: A New Version of the Program for Transmission and Band-Structure Calculations of Photonic Crystals. *Comput. Phys. Commun.* **2000**, *132*, 189–196.
40. Aspnes, D. E.; Studna, A. A. Dielectric Functions and Optical Parameters of Si, Ge, GaP, GaAs, GaSb, InP, InAs, and InSb from 1.5 to 6.0 eV. *Phys. Rev. B* **1983**, *27*, 985–1009.
41. Weingärtner, H.; Sasisanker, P.; Daguene, C.; Dyson, P. J.; Krossing, I.; Slattey, J. M.; Schubert, T. The Dielectric Response of Room-Temperature Ionic Liquids: Effect of Cation Variation. *J. Phys. Chem. B* **2007**, *111*, 4775–4780.
42. Liang, C.-H.; Chen, S.-C.; Qi, X.; Chen, C.-S.; Yang, C.-C. Influence of Film Thickness on the Texture, Morphology and Electro-optical Properties of Indium Tin Oxide Films. *Thin Solid Films* **2010**, *519*, 345–350.
43. Falkovsky, L. A.; Pershoguba, S. S. Optical Far-Infrared Properties of a Graphene Monolayer and Multilayer. *Phys. Rev. B* **2007**, *76*, 153410.
44. Kreibitz, U.; Vollmer, M. *Optical Properties of Metal Clusters*; Springer-Verlag: Berlin, 1995.